The Oxygen Reduction Reaction on Pt: Why Particle Size *and* Inter-particle Distance Matter

Masanori Inaba[a,b], Alessandro Zana[a], Jonathan Quinson[b], Francesco Bizzotto[a], Carsten Dosche[c], Alexandra Dworzak[c, d], Mehtap Oezaslan[c, d], Søren Bredmose Simonsen[e], Luise Theil Kuhn[e] and Matthias Arenz[a*]

[a]Department of Chemistry and Biochemistry, University of Bern, Freiestrasse 3, CH-3012 Bern, Switzerland

[b]Nano-Science Center, Department of Chemistry, University of Copenhagen, Universitetsparken 5, DK-2100 Copenhagen Ø, Denmark

[c]Department of Chemistry, Carl von Ossietzky University of Oldenburg, D-26111 Oldenburg, Germany

[d]Technical Electrocatalysis Laboratory, Institute of Technical Chemistry, Technische Universität Braunschweig, D-38106 Braunschweig

[e]Department of Energy Conversion and Storage, Technical University of Denmark, Fysikvej building 310, 2800 Kgs. Lyngby, Denmark

*Corresponding author

University of Bern, Freiestrasse 3, CH-3012 Bern, Switzerland

Phone: +41 31 631 53 84

Email: matthias.arenz@dcb.unibe.ch

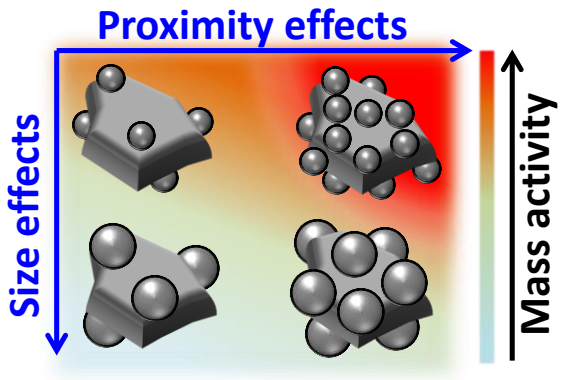

Keywords: Platinum; Oxygen Reduction Reaction (ORR); Particle Size Effect; Inter-particle Distance; *operando* electrochemical X-ray absorption spectroscopy (XAS);

Abstract

Carbon supported Pt based nanoparticles are important electrocatalysts for energy conversion reactions such as the oxygen reduction reaction (ORR). Although this reaction has been extensively studied, the influence of factors such as the particle size and inter-particle distance of the nanoparticle-based or nano-sized electrocatalysts on the ORR activity and durability are not yet fully understood and often intertwined. This lack of understanding is mostly based on the limitation in the synthetic approaches of the electrocatalysts which usually do not allow an independent variation of particle size and inter-particle distance. In the presented work, we succeeded to disentangle both factors using a "colloidal toolbox" approach and have demonstrated an effect of the inter-particle distance on the electronic properties of the nanoparticle via *operando* electrochemical X-ray absorption spectroscopy (XAS).

1. Introduction

In the last decade, the interest in electrocatalyst design has been boosted by the increasing exploitation of regenerative energy in the form of electricity, in particular wind energy and photovoltaic power[1]. The intermittent nature of these energy sources requires suitable energy storage and conversion technologies to be able to align the *"production"* with the

48 *"demand"* of energy. While battery technology shows continuous progress, the storage
49 and re-conversion of electricity in the form of energy carriers such as hydrogen gas still
50 faces substantial challenges[2].
51 For these conversion technologies a fundamental understanding and rational design of
52 electrocatalysts, on which the surface reactions of interest take place, are essential[3]. In
53 state-of-the-art academic electrocatalyst design, typically the focus is on optimizing the
54 surface structure of the catalyst on a nanometer or even atomic scale[4–10]. This approach
55 led to the development of several highly performing electrocatalyst concepts in research,
56 nevertheless, their implementation into realistic conversion devices is not straight-
57 forward[11]. In the presented work, we demonstrate that *mesoscopic properties*[12–14] such as
58 the inter-particle distance of the catalytically active phase on the support material are of
59 equal importance for a rational catalyst design. Investigating the oxygen reduction
60 reaction (ORR) – the cathode reaction in a fuel cell – on different Pt nanoparticle based
61 electrocatalysts, we elucidate the influence of size (and thus structure) of the catalytically
62 active phase (Pt nanoparticles) as well as the mesoscopic property of the average inter-
63 particle distance between these nanoparticles on the carbon support. The influence of the
64 first factor, i.e., the particle or crystallite size of Pt nanoparticles on the ORR is
65 extensively and sometimes controversially discussed in literature[15–23]; investigations date

66 back to the work of Stonehart, Watanabe, Boudart, Kinoshita, Ross, and others[24–29] and
67 cannot be covered here in full length. Interestingly, the metal loading on the support and
68 thus the effective inter-particle distance of the nanoparticles is typically not addressed.
69 An exception is the discussion of reactant diffusion zones around the particles introducing
70 a "territory theory" by Watanabe et al. [28]. Similar models exist in heterogeneous catalysis
71 discussion spill-over and reversed spill-over of reactants between active phase and
72 support material[30,31]. The limited number of studies addressing the influence of the inter-
73 particle distance on catalytic reactions can at least partially be explained by the lack of
74 suitable synthesis strategies to control size and inter-particle distance independently. Only
75 advanced preparation strategies for metal clusters and nanoparticles[32–35] allow such
76 investigations. In previous work, the authors investigated the ORR on size selected Pt
77 clusters prepared by a laser ablation source[34]. It was proposed that at small inter-particle
78 distances an overlap in the electric double layer (EDL) structure at the catalyst-electrolyte
79 interface leads to an increase in ORR activity, i.e. the particle proximity effect of the
80 ORR[14]. Follow up work has demonstrated an improvement in ORR activity at small inter-
81 particle distance also for carbon supported high surface area electrocatalysts[36]. Very
82 recently, it has been shown that the inter-particle distance of Pt nanoparticles deposited
83 on two dimensional as well as three dimensional carbon supports influences the amount

84 of dissolved Pt detected in scanning flow cell (SFC) measurements coupled to online ICP-
85 MS[12]. Density functional theory modeling indicates that proton accumulation caused by
86 the overlap of the EDL (at high particle density) competes with proton depletion caused
87 by the proximity of the nanoparticles to the carbon support[37]. On the other hand, it was
88 suggested in non-catalytic studies that the inter-particle distance (in addition to the
89 particle size) also influences the intrinsic electronic properties of metal nanoparticles. For
90 example, for alkane thiol stabilized colloidal gold nanoparticles a substantial cross-
91 coupling between the particles has been reported when depositing them onto a planar
92 substrate at small separation distances[38]. These observations were interpreted as a result
93 of changes in the screening of charge transfer barriers in the ensembles of nanoparticle
94 due to electron tunneling. It was stated that films of closely separated nanoparticles
95 behave effectively as a collective metal film changing its electronic character[38]. Other
96 reports have even claimed that at very low inter-particle distances, exchange interactions
97 cause otherwise insulating assemblies to become semiconducting, metallic, or
98 superconducting[39].
99 To test the hypothesis that in addition to the particle size, the inter-particle distance
100 influences the intrinsic electronic and thereby the catalytic properties of materials, these
101 parameters need to be adjusted independently. As mentioned above, in order to do so

suitable synthesis strategies are required. While vacuum based laser ablation or magnetron sputtering sources combined with mass selection filters[34,40] offer ultimate control on the particle size, these methods can typically only produce minute sample amounts and require enormous financial and technical investments. By comparison, colloidal approaches[33,40,41] offer similar control on the individual catalyst parameters but can produce more material and are much broader available. In the presented work, we synthesized carbon supported high surface area catalysts (Pt/Vulcan) with various Pt particle sizes and Pt loadings via a toolbox approach that has been developed for this purpose[33,36,42]. The approach builds on the surfactant-free synthesis of colloidal nanoparticles using alkaline ethylene glycol as solvent and reducing agent that was introduced by Wang et al.[43]. The size of the Pt nanoparticles is controlled by varying the NaOH/Pt molar ratio in the colloidal synthesis[44].

2. Experimental section

Chemicals, materials, and gases.

The following chemicals were used in the catalyst synthesis and characterization: ethylene glycol (EG, 99.8 %, Sigma-Aldrich), sodium hydroxide (NaOH, 98.9 %, Fisher Chemical), hexachloroplatinic(IV) acid hexahydrate ($H_2PtCl_6 \cdot 6H_2O$, 99.9 %, Alfa Aesar),

30 % hydrochloric acid (HCl, Suprapur, Merck), 60 % nitric acid (HNO_3, Suprapur, Merck), acetone (99.5+ %, Alfa Aesar), tin(II) chloride dehydrate (> 98 %, Sigma-Aldrich), and platinum standard solution (1000 ± 4 mg L^{-1}, Sigma-Aldrich). Commercial carbon black (Vulcan XC72R, Cabot Corporation, BET area: 235 m^2 g^{-1}) was employed as carbon support in the catalyst synthesis. Deionized (DI) water (resistivity > 18.2 MΩ·cm at room temperature, total organic carbon (TOC) < 5 ppb) from a Milli-Q system (Millipore) was used for acid dilutions, catalyst ink formulation, and the electrochemical cell cleaning. 2-propanol (IPA, 99.7+ %, Alfa Aesar), 70 % perchloric acid ($HClO_4$, Suprapur, Merck), and potassium hydroxide hydrate ($KOH \cdot H_2O$, Suprapur, Merck) were used for catalyst ink formulation and electrolyte preparation. The following gases from Air Liquide were used in electrochemical measurements: Ar (99.999 %), O_2 (99.999 %), CO (99.97 %), and (H_2 99.999 %).

Synthesis of Pt/C catalysts.

50 wt. % Pt/Vulcan electrocatalysts were synthesized via the tool-box approach we previously reported[45]. The synthesis method of the electrocatalyst consists of two main steps: preparation of a suspension of colloidal Pt nanoparticles via an alkaline ethylene glycol (EG) route and a subsequent immobilization of the nanoparticles onto carbon support. A colloidal suspension of Pt nanoparticles (ca. 2 nm in diameter) was synthesized

by mixing 4 mL of a solution of 0.4 M NaOH in EG with 4 mL of a solution of $H_2PtCl_6 \cdot 6H_2O$ at 40 mM in EG (NaOH/Pt molar ratio = 10) in a microwave reaction vessel. The mixture was heated for 3 minutes at 160 °C with a microwave reactor (CEM Discover SP, 100 W heating power). Colloidal suspensions of Pt nanoparticles with larger diameters were synthesized by changing the molar ratio between NaOH and H_2PtCl_6 as we recently reported[44]. Pt nanoparticles with diameter of ca. 3 nm and Pt nanoparticles with diameter of ca. 4 nm were synthesized by using a NaOH solution at 0.22 M (NaOH/Pt molar ratio = 5.5) and a NaOH solution at 0.20 M (NaOH/Pt molar ratio = 5.0) instead of the NaOH solution at 0.4 M (NaOH/Pt molar ratio = 10), respectively.

In order to support the Pt nanoparticles onto a carbon support, 30 mL of 1 M HCl solution was added to 7.3 mL of the colloidal Pt nanoparticles suspension for precipitation. The mixture was centrifuged at 2400 relative centrifugal force (4000 rotations per minute (rpm), Sigma 2-5) for 5 minutes and the supernatant solvent discarded. This washing/centrifugation with 1 M HCl was repeated twice. Then the Pt nanoparticles were re-dispersed in 7 mL of acetone, and 27.5 mg of carbon black (Vulcan XC72R) was added to the suspension. By sonicating the mixture in an ultrasonic bath (Ultrasonic cleaner, VWR) for 1 hour, the acetone was evaporated, and a dried powder of Pt nanoparticles supported on carbon (Pt/Vulcan) was obtained. The dried powder was re-dispersed into

156 water and sonicated for 10 minutes. The Pt/C catalyst powder was filtered and washed
157 with 200 mL of DI water, and then dried at 100 °C in air. Pt/C catalysts with different Pt
158 nominal loadings (10, 20, 30, 40, 60, and 70 wt. %) were prepared by changing the
159 amount of the carbon support mixed with the Pt nanoparticles in the immobilization step.

160 ***Characterization of Pt/C catalysts.***

161 The particle size distribution of Pt nanoparticles immobilized on the carbon support was
162 determined by transmission electron microscopy (TEM, Tecnai Spirit, FEI, 80 kV or Jeol
163 2100; Jeol 3000F for HR-TEM). The size analysis was performed using ImageJ software
164 (without automated processing of the image) by measuring the size of more than 80
165 nanoparticles by taking micrographs in 5 different areas of the TEM grid. The mean
166 number diameter (d_{MN}) and the mean area diameter (d_{MA}) of the Pt nanoparticles were
167 calculated using the following equations:

168 $$d_{MN} = \frac{\sum d_i}{N}$$

169 $$d_{MA} = \frac{\sum (A_i d_i)}{\sum A_i} = \frac{\sum (\pi d_i^3/4)}{\sum (\pi d_i^2/4)}$$

170 where d_i, N, A_i are the diameters of the individual particles, the number of the particles,
171 and the surface area of the individual particle, respectively.

172 The actual Pt loadings of the catalysts were evaluated by using UV-Vis spectroscopy[46].
173 For sample preparation, 2.0 mg of catalyst powder was weighed in a ceramic crucible and

heated in a muffle furnace (air, 900 °C, 30 min) to burn off the carbon support. Afterward 4 mL of aqua regia (mixture of 30 % HCl and 65 % HNO_3 in a volume ratio of 1:3) was added in the crucible and heated for 90 minutes on a heating plate at ca. 80 °C to digest platinum. After the digestion the final volume of the aqua regia sample was adjusted to 100 mL with DI water. 1 mL of the aqua regia sample, 0.25 mL of 1 M $SnCl_2$ in 4 M HCl, and 0.75 mL of 2 M HCl were mixed in a quartz cuvette and a UV-Vis spectrum of the sample mixture was measured. Subsequently 5 µL of Pt standard solution (1000 ppm) was added to the sample solution and a UV-Vis spectrum of the sample mixture was measured again. The addition of the platinum standard solution and the measurements were repeated 4 times. The absorbance at 402 nm was plotted against the concentration of the added platinum to obtain a calibration curve. Finally, the concentration of platinum in the aqua regia sample was determined from the x-intercept of the calibration curve.

Inter-particle distance (edge-to-edge distance) of Pt nanoparticles was estimated using the following equation[36]:

$$d_{ip} = \sqrt{A/N} - d_{NP}$$

where d_{ip}, A, N, and d_{NP} are inter-particle distance, BET surface area of the carbon support, number of Pt nanoparticles, and diameter of Pt nanoparticles, respectively. The mean area diameters that were obtained by analyzing the TEM images of 30 wt.% Pt/Vulcan

192 catalysts (see Figure 1) were used as d_{NP} for each respective nanoparticle size. The Pt
193 particle size, nominal Pt loading, actual Pt loading, and inter-particle distance based on
194 actual loading of each Pt/C catalyst are summarized in Table S1.

195 ***RDE measurements.***

196 6.27 mg of the homemade 50 wt. % Pt/Vulcan catalyst powder was mixed with 8 mL of
197 IPA:DI water (1:3, v:v) mixed solvent to formulate a catalyst ink. The Pt concentration in
198 the catalyst ink was always kept at 0.392 mg_{Pt} mL^{-1} for all Pt/Vulcan catalysts with
199 different Pt loadings. A small amount of 1 M KOH solution (~8 μL) was added to adjust
200 the pH of the ink to be around 10[47]. The glass vial containing the mixture was placed in
201 an ultrasonic bath filled with cold water (< 5 °C) and sonicated for 15 minutes.
202 A glassy carbon (GC) disc electrode (5 mm in diameter, 0.196 cm^2 in geometric area) was
203 polished to mirror finish using alumina oxide paste (0.3 and 0.05 μm AP-D suspension,
204 Struers), and cleaned ultrasonically in DI water. A 5 μL aliquot of the catalyst ink was
205 pipetted onto the GC electrode leading to a Pt loading of 10 μg_{Pt} cm^{-2}. Subsequently the
206 ink on the GC electrode was dried under Ar gas flow humidified with mixture of IPA and
207 DI water (17:3, v:v) in a bubbler[46]. After the drying, the surface of the GC electrode was
208 checked with the help of a CCD camera to confirm that the electrode surface was
209 uniformly covered with the catalyst thin film.

An in-house Teflon cell based on a three-compartment configuration was employed in all electrochemical measurements[48]. A platinum mesh was used as a counter electrode. A saturated calomel electrode (B3510+, Schott) was employed as a reference electrode and placed in a sub-compartment separated by a Nafion membrane to avoid the contamination of chloride ions into the main compartment. All potentials in this study are referred to the reversible hydrogen electrode (RHE) potential, which was experimentally determined for each measurement series. The Teflon cell and components were soaked in mixed acid (H_2SO_4:HNO_3 = 1:1, v:v) overnight. Subsequently the Teflon cell and other components were rinsed thoroughly by DI water, and boiled in DI water twice.

All electrochemical measurements were performed using a computer controlled potentiostat (ECi 200, NordicElectrochemistry) and the Teflon cell with an RDE rotator (EDI101, Radiometer Analytical). The measurements were performed in 0.1 M $HClO_4$ solution at room temperature. Prior to the measurements, the electrolyte was de-aerated by purging with Ar gas, and the catalysts were cleaned by potential cycles between 0.05 and 1.20 V at a scan rate of 500 mV s^{-1} until a stable cyclic voltammogram was observed (typically 30–50 cycles). The electrochemical surface area (ECSA) of the catalyst was determined by conducting CO stripping voltammetry[21]. The working electrode was held at 0.05 V during purging CO through the electrolyte followed by saturating with Ar. The

ECSA was calculated from the CO oxidation charge recorded at a scan rate of 50 mV s^{-1} using conversion coefficient of 390 μC cm^{-2}_{Pt}. To determine the ORR activity, linear sweep voltammetry (LSV, positive scan) was conducted in O_2-saturated electrolyte at a scan rate of 50 mV s^{-1} and a rotation speed of 1600 rpm. The polarization curves were corrected for the nonfaradaic background by subtracting the cyclic voltammograms (CVs) recorded in Ar-purged electrolyte at the identical scan rate. Furthermore, the solution resistance (R_{sol}) between the working electrode and the Luggin capillary (~23 Ω) was determined using an AC signal (5 kHz, 5 mV) and thereafter compensated for using the potentiostat´s analog positive feedback scheme. The resulting effective solution resistance was less than 3 Ω for each experiment. The ORR kinetic current density j_k was extracted from the measured current density j using Koutecky-Levich equation described as: $1/j=1/j_k+1/j_l$

where j_l is diffusion limiting current density. In this study, the ORR activity of the catalysts was always evaluated at 0.9 V vs. RHE.

XAS measurements.

XAS measurements were carried out at the SuperXAS (X10DA) beamline, Swiss Light Source (SLS), Switzerland (energy of storage ring 2.4 GeV; beam current 400 mA) and at the B18 beamline of the Diamond Light Source, UK (energy of storage ring 3 GeV;

246 beam current 300 mA). N_2 was used to fill both ionization chambers for the detection of
247 incident (I_0) and transmitted (I_1 and I_2) X-ray radiation. For *ex situ* XAS measurements,
248 a mixture of Pt/Vulcan powders and cellulose as a binder was pressed to form a
249 homogeneous pellet with a uniform thickness. The *operando* electrochemical XAS
250 experiments were performed in a home-made spectro-electrochemical flow cell with a
251 three-electrode configuration. The basic cell design has been reported elsewhere[49]. Some
252 modifications like electrolyte thickness, diameter of channels, compartment of the
253 reference electrode, etc. were made to optimize the signal-to-noise ratio for the XAS
254 measurements at the Pt L_3 edge in transmission mode. A dispersion of Pt/Vulcan in IPA
255 and water was dropped onto a carbon paper. After drying, the resulting catalyst film was
256 used as working electrode. A graphite foil was applied as counter electrode, a non-leakage
257 Ag/AgCl (3 M KCl, EDAQ) serves as a reference electrode. The electrolyte solution (0.1
258 M $HClO_4$) at a constant rate flew from a reservoir to the cell and then to the waste
259 container. XAS data were analyzed by FEFFIT software suite[50]. The data processing
260 included the background subtraction, edge step normalization and conversion of the
261 energy units (eV) to photoelectron wave vector k units ($Å^{-1}$) by assigning the
262 photoelectron energy origin, E_0, corresponding to k = 0, to the first inflection point of the
263 absorption edge. Extended X-ray absorption fine structure (EXAFS) spectra were

Fourier-transformed to obtain pseudo radial structure functions (RSFs). The amplitude reduction factor (S_0^2) was obtained from the fit of the EXAFS spectrum of a Pt foil to be 0.82.

XPS measurements.

X–ray photoelectron spectra (XPS) were measured using an ESCALAB 250 Xi instrument (Thermo Fisher, East Grinsted, UK) with monochromatized Al Kα (hν = 1486.6 eV) radiation and an in-lens electron source was used for charge compensation. The high-resolution spectrum for Pt 4f was measured with a pass energy of 10 eV, 50 ms dwell time and 0.02 eV steps referenced to graphitic carbon at 284.3 eV. Peak fitting was performed with the XPS Peak41 software using a Gaussian Lorential (G/L) mixed function after a Shirley background subtraction.

3. Results and discussions

As an example, Figure 1 displays TEM micrographs of 30 wt. % Pt/Vulcan catalysts where the NaOH/Pt molar ratio for the Pt nanoparticle preparation was 10, 5.5, and 5.0, respectively. High resolution (HR) TEM signifies that all nanoparticles are highly crystalline (see insets of HR-TEM of the unsupported face centered cubic (*fcc*) Pt nanoparticles) and vary in particle size. The mean number diameters (d_{MN}) increase from

282 1.7 to 2.5, and 3.3 nm, respectively, and the mean area diameters (d_{MA}) from 1.8 to 2.8,

283 and 3.9 nm, respectively.

284

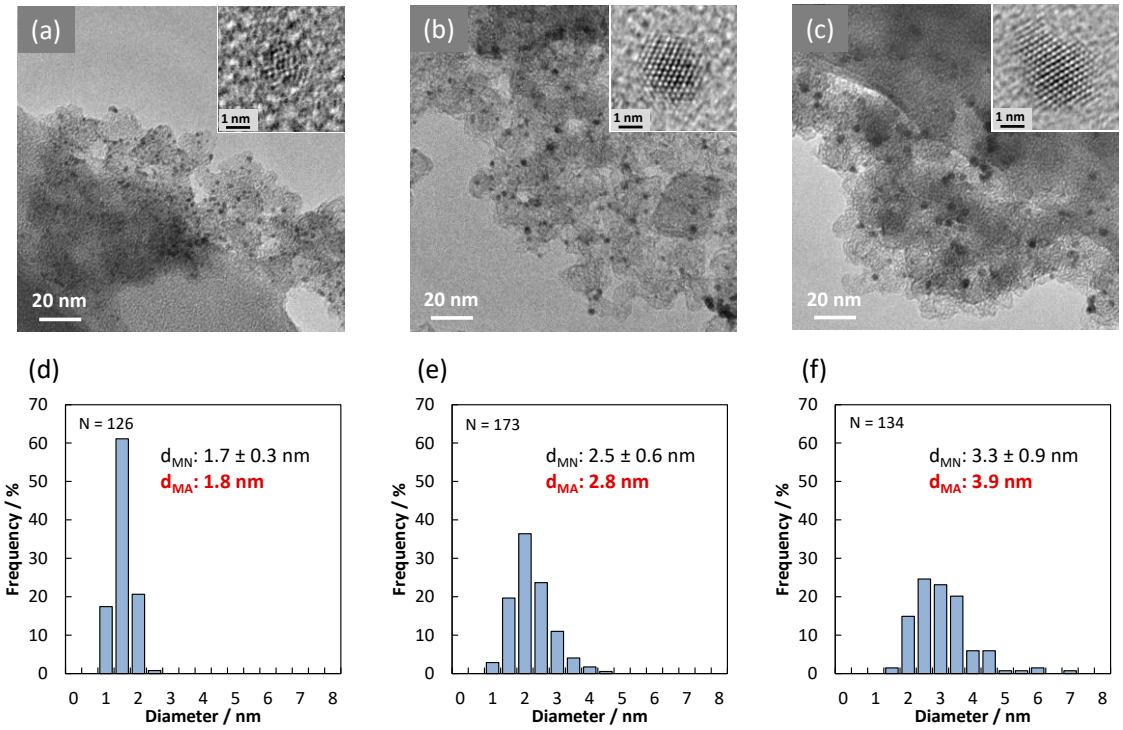

285

286 Figure 1. TEM micrographs of 30 wt. % Pt/Vulcan catalysts (a-c) and respective particle
287 size distributions (d-f). NaOH/Pt molar ratios for the Pt nanoparticle synthesis were 10
288 (a, d), 5.5 (b, e), and 5.0 (c, f), respectively. The insets show HR-TEM micrographs of
289 unsupported Pt nanoparticles. N, d_{MN}, and d_{MA} stand for number of analyzed Pt
290 nanoparticles, mean number diameter, and mean area diameter, respectively.

291

292 Varying the inter-particle distance at constant particle size is a more challenging exercise.

293 By mixing the colloidal nanoparticle suspensions with different amounts of Vulcan

294 carbon support we varied the nominal metal loading between 10 – 70 wt. % Pt/Vulcan for

295 each colloidal nanoparticle suspension. Figure 2 displays TEM micrographs of 10, 30, 50,

296 and 70 wt. % Pt/Vulcan catalysts prepared from the colloidal suspension of 1.8 nm sized
297 Pt nanoparticles. It is seen that the Pt nanoparticles are highly dispersed on the carbon
298 support up to the nominal Pt loading of 50 wt. % (Figure 2 (a) – (c)), whereas some minor
299 agglomeration of Pt nanoparticles can be observed at very high nominal metal loadings
300 like 70 wt. % Pt/Vulcan (Figure 2 (d)). The mean diameter of the Pt nanoparticles is
301 almost independent of the metal loading. Only a small increase in the number of slightly
302 larger Pt particles (> 2.5 nm) is observed for very high loading (70 wt. %, see Figure S1).
303

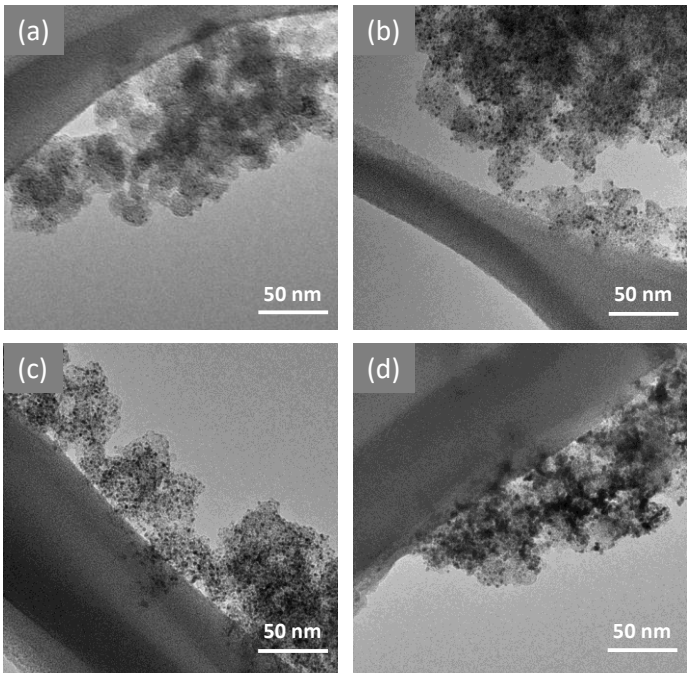

304
305 Figure 2. TEM micrographs of Pt/Vulcan catalysts prepared by using 1.8 nm sized Pt
306 nanoparticles (NaOH/Pt molar ratio = 10). The nominal Pt loadings are (a) 10 wt. %, (b)
307 30 wt. %, (c) 50 wt. %, and (d) 70 wt. %, respectively.
308

309 Varying the metal loading with constant particle size leads to a systematic change in inter-
310 particle distance on the carbon support. The successful variation of the inter-particle
311 distance at constant particle size without agglomeration is best scrutinized by determining
312 the electrochemically active surface area (ECSA) as function of the metal loading. If the
313 ECSA is independent of the metal loading the absence of particle agglomeration is
314 confirmed. The average inter-particle distance can then be calculated from the BET
315 surface area of the carbon support, the number of Pt nanoparticles on the support as well
316 as the diameter of Pt nanoparticles, see experimental section. In Figure 3, the results of
317 the electrochemical characterization via rotating disk electrode (RDE) measurements are
318 summarized (representative cyclic voltammograms and CO stripping voltammograms of
319 the Pt/C catalysts and the analysis of the cyclic voltammograms are displayed in the
320 supplementary information in Figures S2, S3, and S4, respectively.). In Figure 3, each
321 color represents a different Pt particle size, i.e., 1.8, 2.8, and 3.9 nm in average diameter.
322 It is seen that the ECSA is indeed almost constant for each Pt particle size independent of
323 the metal loading. Only with a very large number of nanoparticles immobilized on the
324 support (high metal loadings and small nanoparticles) a substantial decrease in ECSA is
325 observed, indicating particle agglomeration during the particle immobilization step of the
326 catalyst preparation. In these cases, particle size and inter-particle distance effects are

interwoven due to the limitations in catalyst synthesis. In the other cases, the ECSA values for each sample are consistent with the individual particle size determined from the TEM data assuming that 67 % of the particle surface of the supported Pt nanoparticles is electrochemically accessible (see Figure S5).

The influence of particle size and inter-particle distance on the ORR activity is demonstrated in Figures 3(b) and 3(c). It is seen that the Pt surface area-based specific ORR activity (SA) (i.e., the reaction rate normalized to the number of catalytically active sites) depends on the particle size as well as on the inter-particle distance. For smaller (1.8 nm) Pt nanoparticles the influence of the inter-particle distance on the SA is most prominent. The SA at 0.9 V_{RHE} increases by ca. 220 % (all values are rounded) when the average inter-particle distance is decreased from 11.5 nm to 1.4 nm. This trend is opposite to the one reported by Watanabe et al. in the 1980's where the SA decreases with a decrease in the inter-particle distance between 14-20 nm[28]. It should be noted that the inter-particle distance values are not exact when Pt agglomeration is suspected and the ECSA is decreased (60 and 70 wt.% for the 1.8 nm sized Pt particles) because its influence is not considered in the inter-particle distance calculation. However, in the present work, even if the data points where Pt agglomeration is suspected are discarded, the SA still increases by 170 % with decreasing inter-particle distance from 11.5 nm to 2.7 nm. The

345 increase in SA with the particle size can be extracted based on the activity values at high
346 inter-particle distance. Here, the nanoparticles can be considered as individual, supported
347 particles. Based on the data at 0.9 V_{RHE}, the SA increases by 190 % when increasing the
348 average particle size from 1.8 nm to 3.9 nm. This trend of the SA with the particle size is
349 in good agreement with the results obtained from the measurements of sputtered Pt/GC
350 (glassy carbon) model electrodes[23] and Nafion-free measurements of carbon supported
351 Pt/C catalysts[51] reported in literature, see Figure 4. In general, this "intrinsic" particle size
352 effect can be related to a shift in the reduction potential of Pt oxide species, see ref.[19] and
353 Figure 5. The results demonstrate that the inter-particle distance is equally important as
354 the particle size for the SA of the ORR. Analyzing the Tafel plots of the SA with changing
355 the inter-particle distance at same loadings, see Figure S6, demonstrates that the Tafel
356 slopes of the respective catalysts are identical which confirms that these results are not
357 due to experimental artifacts in the measurement but due to changes in reaction kinetics.
358
359 The trend for the mass activity (MA), i.e., the reaction rate per mass of Pt, is more
360 complicated as the MA depends on the SA and the ECSA (MA = SA · ECSA). At large
361 inter-particle distance (low metal loading) the MA of the 1.8 and 2.8 nm Pt nanoparticle
362 catalysts is the same, while the 3.9 nm nanoparticle catalyst has a slightly lower MA.

However, decreasing the inter-particle distance (increasing metal loading), the MA of the 1.8 nm Pt nanoparticle catalyst exhibits a maximum due to particle agglomeration (see Figure 2d). First, the MA increases due to the particle proximity effect and then decreases due to a loss in ECSA because of agglomeration. In summary, the optimization of particle size and inter-particle distance in the here prepared catalyst leads to a maximum MA of 1300 A g^{-1} at 0.9 V_{RHE} for the Pt/Vulcan catalyst, which is more than twice of the MA we determined for standard commercial Pt/C catalysts[15].

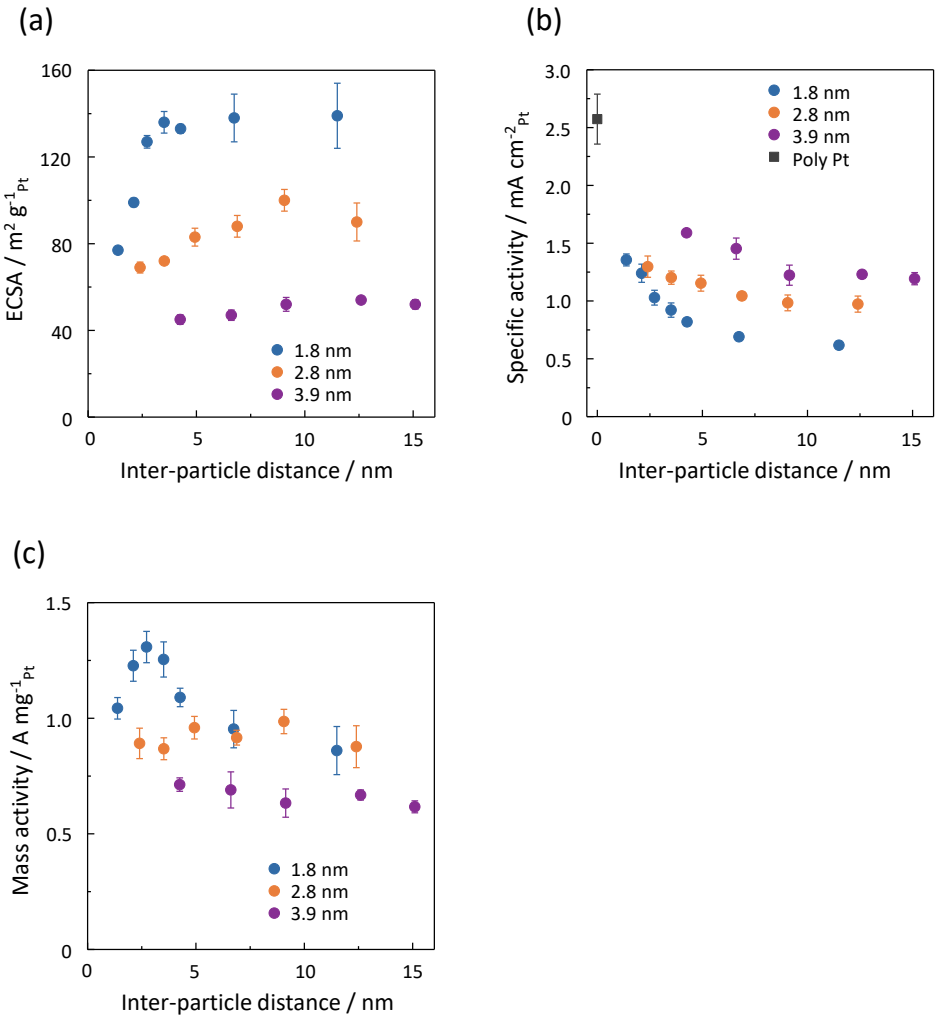

371

372 Figure 3. ECSA (a), ORR specific activity (SA) at 0.9 V_{RHE} (b) and ORR mass activity
373 (MA) at 0.9 V_{RHE} (c) of the Pt/Vulcan catalysts with various Pt loadings and Pt
374 nanoparticle sizes determined from the RDE measurements. Each measurement was
375 repeated more than 4 times and error bars show 95 % confidence interval.

376

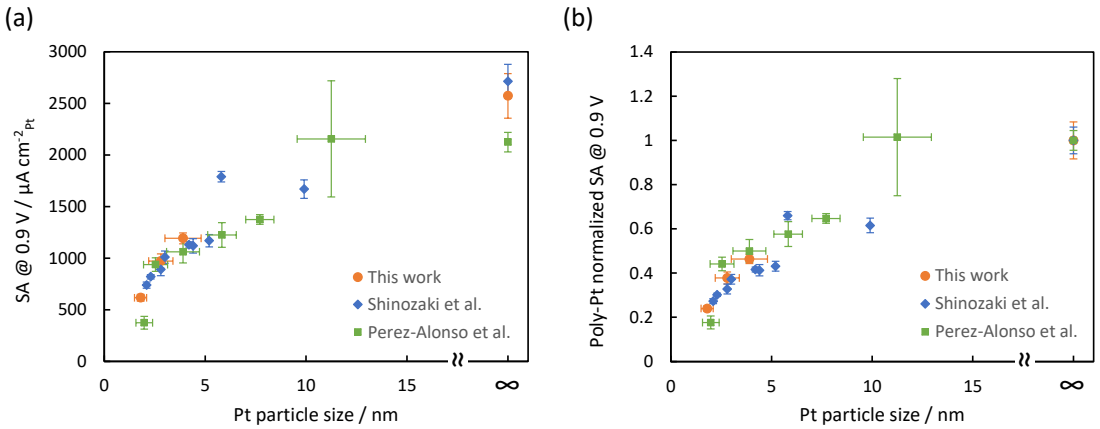

Figure 4. (a) Particle size dependence of the specific ORR activity (SA) at 0.9 V vs. RHE in 0.1 M $HClO_4$ electrolyte measured in this study in comparison with literature values. The SA values for this study were taken from Figure 5a. (b) Normalized SA dependence on the particle size obtained in this study as well as found in literature. Literature values were taken from Shinozaki et al.[25] and Perez-Alonzo et al.[24].

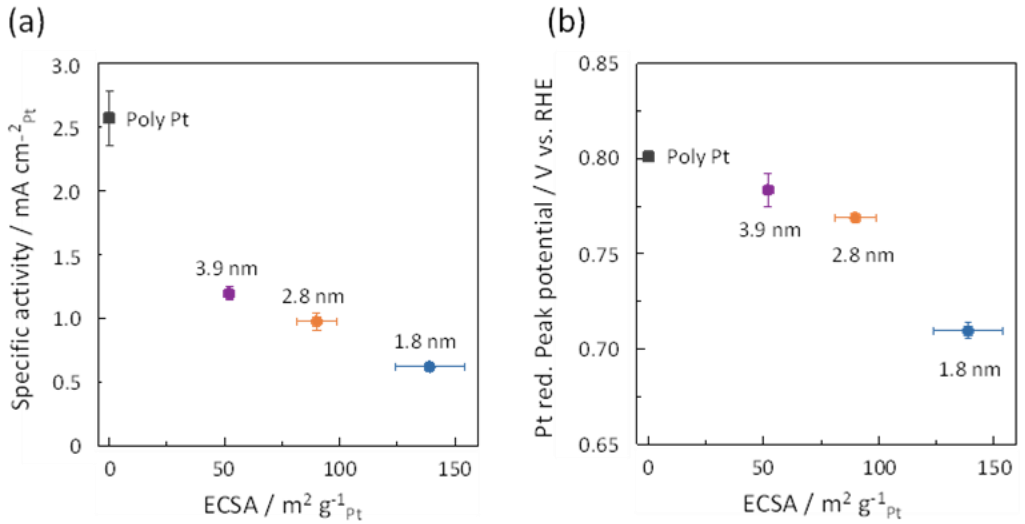

Figure 5. "Intrinsic" particle size effects on (a) ORR specific activity and (b) Pt-oxide reduction peak potential. Measured values of the 3 different sized Pt nanoparticles at the lowest Pt loading (10, 20, and 30 wt. % in nominal Pt loading for 1.8, 2.8, and 3.9 nm

390 sized Pt nanoparticles, respectively) are plotted as a function of ECSA. The experimental
391 data for polycrystalline Pt is added to the plot at an ECSA value of 0.

392

393 As mentioned above, different effects can cause the observed particle proximity effect. In
394 literature effects ranging from changes in the EDL structure at the catalyst-electrolyte
395 interface[14] to changes in the intrinsic electronic properties of the nanoparticles due to a
396 screening of the charge transfer barrier due to electron tunneling[38] are discussed.
397 Previously, it has been reported that for smaller particle sizes the Pt-OH reduction peak
398 potential in cyclic voltammograms (CVs) of Pt/C measured in Ar purged electrolyte shifts
399 to more positive values with decreasing inter-particle distance[36]. This behavior which is
400 often associated with higher ORR activity[19] is here confirmed with the prepared Pt/Vulcan
401 catalysts, see Figure 6. In Figure 6, it is seen that the reduction peak potential value of the
402 Pt nanoparticles approaches that of bulk Pt with a decrease in the inter-particle distance.
403 The observed trends in oxophilicity suggest that the surface properties of the Pt
404 nanoparticles become more "bulk-like" with decreasing the inter-particle distance.
405 Interestingly, the proximity effect on the Pt reduction peak potential as well as the increase
406 in SA are the most prominent for small (1.8 nm) Pt nanoparticles. This could be related
407 to the fact that the "larger" Pt nanoparticles are more "bulk-like" to begin with (i.e., at
408 large inter-particle distance). A similar trend, i.e., indications that the surface properties

409 of the Pt nanoparticles become more “bulk-like” with decreasing the inter-particle
410 distance can be seen by an analysis of the CO oxidation peaks in the CO stripping
411 voltammograms (Figure S7). While the peak position of the CO oxidation peaks is
412 independent of the inter-particle distance, its width decreases with decreasing inter-
413 particle distance.

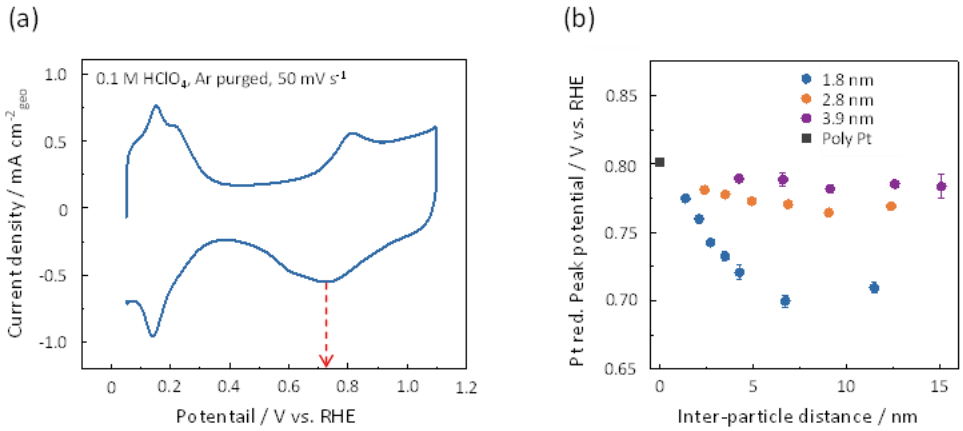

414

415 Figure 6. (a) Typical cyclic voltammogram of Pt/Vulcan catalyst measured in Ar-purged
416 0.1 M $HClO_4$ electrolyte. In this case, Pt reduction peak is seen at around 0.75 V. (b)
417 Reduction peak potential of the Pt/Vulcan catalysts with various metal loadings and
418 nanoparticle sizes.

419

420 The trend in oxophilicity can also be observed in X-ray photoelectron spectroscopy (XPS)
421 and X-ray absorption spectroscopy (XAS). As previously reported[12] e*x situ* Pt 4f XPS
422 spectra, Figure S8, demonstrate that after preparing Pt/Vulcan catalysts with the same
423 nanoparticle size (1.8 nm), but different inter-particle distance and exposing them to air,
424 their degree of oxidation state decreases with decreasing inter-particle distance

425 (increasing metal loading). The same trend in reduced oxophilicity with decreasing inter-
426 particle distance is observed in *ex situ* recorded extended X-ray absorption fine structure
427 (EXAFS) and X-ray absorption near edge structure (XANES) measurements, see Figures
428 S9, S10 and Table S2. Decreasing the inter-particle distance (increasing metal loading)
429 the determined Pt-O coordination numbers decreases, while the Pt-M coordination
430 numbers stay almost constant with slight variations.)[12]. Concurrently, the white line
431 intensity in the Pt L_3 edge XANES spectra decreases[12]. One could argue that the
432 established trend in reduced oxophilicity with decreasing inter-particle distance is
433 observed *ex situ* after exposure to air and therefore not relevant for the electrochemical
434 performance.
435 Therefore, considerable effort was undertaken to establish *operando* spectroscopic
436 evidence of the particle proximity effect in addition to the trends of the specific ORR
437 activity and the shift in the Pt-OH reduction peak potential obtained from the CVs. Here,
438 to the best of our knowledge we demonstrate for the first time such evidence using
439 *operando* electrochemical XAS. In Figure 7, it is shown that XAS spectra recorded under
440 potential control reveal the same trend in oxophilicity with inter-particle distance as the
441 *ex situ* data. Plotting the ratio of the Pt-O and Pt-Pt coordination numbers extracted from
442 the *operando* Pt L_3 edge EXAFS spectra as a function of the electrode potential for the

443 different Pt/Vulcan catalysts it can be seen that the degree of oxidation (i.e., at fixed
444 electrode potential) changes with decreasing the inter-particle distance (increasing the
445 metal loading). Furthermore, the hysteresis[52,53], i.e., difference in oxide coverage when
446 stepping the electrode potential in positive or negative direction, is less pronounced with
447 the highly loaded Pt/Vulcan catalyst. The data clearly demonstrate that a small inter-
448 particle distance of the Pt nanoparticles supported on the Vulcan leads to a lower oxide
449 coverage, which in turn leads to an improved specific ORR activity.
450

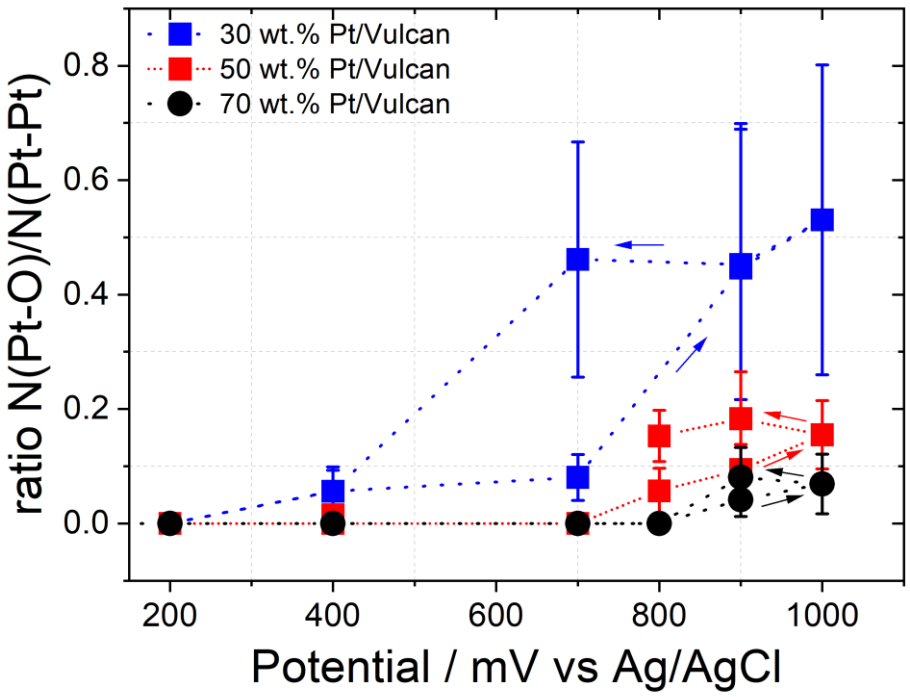

451
452 Figure 7. *Operando* electrochemical EXAFS data of 1.8 nm Pt/Vulcan catalysts with
453 different metal loadings, 30 wt. %, 50 wt. %, and 70 wt. %, that results in different inter-
454 particle distances. The plots show the calculated ratio of both coordination numbers N(Pt-

O) and N(Pt-Pt) as a function of the applied electrode potential. The arrows indicate if the spectra were recorded coming from a lower or higher electrode potential. Measurements with 10 wt. % were not feasible due to too thick catalyst layers required for good quality XAS spectra. The error bars indicate the standard error obtained from the fit analysis using the EXAFS equation.

4. Conclusions

In an extensive effort of varying particle size and inter-particle distances for Pt based ORR catalysts independent of each other, we manage to disentangle the influence of the inter-particle distance and the particle size on the specific ORR activity. It is found that both effects are equally important when optimizing the specific ORR activity for a catalyst. Larger Pt nanoparticles exhibit a higher specific ORR activity than smaller ones, when the inter-particle distance is large. However, the specific ORR activity of Pt nanoparticles can be improved when immobilizing them at high coverage on a carbon support. This influence of the inter-particle distance on the catalytic ORR activity is most pronounced for smaller nanoparticles as compared to larger ones. Although high metal loadings also favour particle agglomeration during synthesis, in particular for small nanoparticles a clear increase in activity with the inter-particle distance is seen when limiting the discussion to the metal loadings where the ECSA proofs constant dispersion (and thus constant particle size). As a consequence, we observe the highest mass normalized ORR activity for small nanoparticles at high coverage.

As compared to the long-discussed particle size effect, inter-particle distance effects are a fairly recent topic in catalysis and the underlying mechanisms have been addressed by only few research groups. Essentially two explanation models have been suggested in literature. One focussing on the effect of the inter-particle distance on the EDL structure[14,37] and one focusing on electronic cross-coupling effects as a result of changes in the screening of charge transfer barriers between the particles[38].

Concomitantly with the increase in ORR activity with decreasing inter-particle distance, a decrease in oxophilicity is observed. In the present work we could for the first time demonstrated the correlation of the particle proximity effect to a reduced oxophilicity of the Pt nanoparticles by *operando* electrochemical XAS. Although none of the explanation models of the particle proximity effect can be excluded. Two findings point towards the importance of electronic cross coupling effects. First, the particle proximity effect is clearly more pronounced at small nanoparticles. Second, the same trend of reduced oxophilicity at low inter-particle distance is observed in *operando* XAS and *ex situ* XAS and XPS spectroscopy. Therefore, we propose that the electronic properties of nanoparticles are influenced by the inter-particle distance in a more fundamental way than only by a change in the EDL. As a consequence, mesoscopic properties such as the inter-particle distance are an important design parameter for catalytic processes.

Acknowledgments

This work was supported by the Swiss National Science Foundation (SNSF) via the project No. 200021_184742. M.I. and M.A. gratefully acknowledge support from Toyota Central R&D Labs., Inc. The German Research Foundation (DFG) is acknowledged for funding the XPS ESCALAB 250 Xi (INST 184/144-1 FUGG). A.D. and M.O. have received funding from the DFG (FOR2213, TP9) and the Federal Ministry of Education and Research (BMBF, ECatPEMFC, FKZ 03SF0539). The SLS and Diamond Light Source are acknowledged for the provision of beamtime at the SuperXAS beamline (project ID 20161303) and beamline B18 (proposal SP12746), respectively.

Correspondence and requests for materials should be addressed to Matthias Arenz.

Author contributions:

M.I., A.Z, and M.A. designed the electrochemical measurements. M.I. performed and analysed the RDE and TEM measurements. S.B.S. and J.Q. performed and analysed the HR-TEM measurements. M.O., A.D., J.Q., A.Z., F.B. performed the XAS measurements, that were analysed by M.O. and A.D. C.D. recorded the XPS measurements that were

analysed by A.Z. M.I. and M.A. wrote the first draft of the paper. All authors participated in writing the final draft of the paper.

Statement on competing financial interest's:

There are no financial interests of the authors involved in this work.

Additional information:

Supplementary information accompanies this paper.

Relationship between particle diameter and electrochemically active surface area, Tafel plots, Pt reduction peak potentials, *Ex situ* Pt 4f XPS spectra, *Ex situ* Pt L3 XAS spectra, FT-transformed magnitudes of the k2-weighted EXAFS spectra, and results from fitting of the *ex situ* EXAFS spectra

References

(1) She, Z. W.; Kibsgaard, J.; Dickens, C. F.; Chorkendorff, I.; Nørskov, J. K.; Jaramillo, T. F. Combining Theory and Experiment in Electrocatalysis: Insights into Materials Design. *Science*. 2017. https://doi.org/10.1126/science.aad4998.

(2) Stamenkovic, V. R.; Strmcnik, D.; Lopes, P. P.; Markovic, N. M. Energy and Fuels

from Electrochemical Interfaces. *Nat. Mater.* **2016**, *16* (1), 57–69. https://doi.org/10.1038/nmat4738.

(3) Stephens, I. E. L.; Rossmeisl, J.; Chorkendorff, I. Toward Sustainable Fuel Cells. *Science (80-.).* **2016**, *354*, 1378–1379. https://doi.org/10.1126/science.aal3303.

(4) Chattot, R.; Le Bacq, O.; Beermann, V.; Kühl, S.; Herranz, J.; Henning, S.; Kühn, L.; Asset, T.; Guétaz, L.; Renou, G.; Drnec, J.; Bordet, P.; Pasturel, A.; Eychmüller, A.; Schmidt, T. J.; Strasser, P.; Dubau, L.; Maillard, F. Surface Distortion as a Unifying Concept and Descriptor in Oxygen Reduction Reaction Electrocatalysis. *Nat. Mater.* **2018**, *17*, 827–833. https://doi.org/10.1038/s41563-018-0133-2.

(5) Calle-Vallejo, F.; Tymoczko, J.; Colic, V.; Vu, Q. H.; Pohl, M. D.; Morgenstern, K.; Loffreda, D.; Sautet, P.; Schuhmann, W.; Bandarenka, A. S. Finding Optimal Surface Sites on Heterogeneous Catalysts by Counting Nearest Neighbors. *Science (80-.).* **2015**, *350* (6257), 185–189. https://doi.org/10.1126/science.aab3501.

(6) Hong, W. T.; Risch, M.; Stoerzinger, K. A.; Grimaud, A.; Suntivich, J.; Shao-Horn, Y. Toward the Rational Design of Non-Precious Transition Metal Oxides for Oxygen Electrocatalysis. *Energy and Environmental Science*. 2015, pp 1404–1427. https://doi.org/10.1039/c4ee03869j.

(7) Cui, C.; Gan, L.; Heggen, M.; Rudi, S.; Strasser, P. Compositional Segregation in

548 Shaped Pt Alloy Nanoparticles and Their Structural Behaviour during
549 Electrocatalysis. *Nat. Mater.* **2013**, *12* (8), 765–771.
550 https://doi.org/10.1038/nmat3668.
551 (8) Stamenkovic, V. R. V. R.; Mun, B. S. B. S. B. S.; Arenz, M.; Mayrhofer, K. J. J. K.
552 J. J.; Lucas, C. A. C. A.; Wang, G.; Ross, P. N. P. N.; Markovic, N. M. N. M. N. M.
553 Trends in Electrocatalysis on Extended and Nanoscale Pt-Bimetallic Alloy
554 Surfaces. *Nat. Mater.* **2007**, *6* (3), 241–247. https://doi.org/10.1038/nmat1840.
555 (9) Sievers, G. W.; Jensen, A. W.; Quinson, J.; Zana, A.; Bizzotto, F.; Oezaslan, M.;
556 Dworzak, A.; Kirkensgaard, J. J. K.; Smitshuysen, T. E. L.; Kadkhodazadeh, S.;
557 Juelsholt, M.; Jensen, K. M. Ø.; Anklam, K.; Wan, H.; Schäfer, J.; Čépe, K.;
558 Escudero-Escribano, M.; Rossmeisl, J.; Quade, A.; Brüser, V.; Arenz, M. Self-
559 Supported Pt–CoO Networks Combining High Specific Activity with High Surface
560 Area for Oxygen Reduction. *Nat. Mater.* **2021**, *20* (2), 208–213.
561 https://doi.org/10.1038/s41563-020-0775-8.
562 (10) Gatalo, M.; Ruiz-Zepeda, F.; Hodnik, N.; Dražić, G.; Bele, M.; Gaberšček, M.
563 Insights into Thermal Annealing of Highly-Active PtCu3/C Oxygen Reduction
564 Reaction Electrocatalyst: An in-Situ Heating Transmission Electron Microscopy
565 Study. *Nano Energy* **2019**, *63*, 103892.

https://doi.org/10.1016/j.nanoen.2019.103892.

(11) Han, B.; Carlton, C. E.; Kongkanand, A.; Kukreja, R. S.; Theobald, B. R.; Gan, L.; O'Malley, R.; Strasser, P.; Wagner, F. T.; Shao-Horn, Y. Record Activity and Stability of Dealloyed Bimetallic Catalysts for Proton Exchange Membrane Fuel Cells. *Energy Environ. Sci.* **2015**, *8* (1), 258–266. https://doi.org/10.1039/c4ee02144d.

(12) Sandbeck, D. J. S.; Secher, N. M.; Inaba, M.; Quinson, J.; Sørensen, J. E.; Kibsgaard, J.; Zana, A.; Bizzotto, F.; Speck, F. D.; Paul, M. T. Y.; Dworzak, A.; Dosche, C.; Oezaslan, M.; Chorkendorff, I.; Arenz, M.; Cherevko, S. The Dissolution Dilemma for Low Pt Loading Polymer Electrolyte Membrane Fuel Cell Catalysts. *J. Electrochem. Soc.* **2020**, *167* (16), 164501. https://doi.org/10.1149/1945-7111/abc767.

(13) Du, J.; Quinson, J.; Zhang, D.; Bizzotto, F.; Zana, A.; Arenz, M. Bifunctional Pt-IrO2 Catalysts for the Oxygen Evolution and Oxygen Reduction Reactions: Alloy Nanoparticles versus Nanocomposite Catalysts. *ACS Catal.* **2021**, *11* (2), 820–828. https://doi.org/10.1021/acscatal.0c03867.

(14) Nesselberger, M.; Roefzaad, M.; Fayçal Hamou, R.; Ulrich Biedermann, P.; Schweinberger, F. F.; Kunz, S.; Schloegl, K.; Wiberg, G. K. H.; Ashton, S.; Heiz,

584 U.; Mayrhofer, K. J. J.; Arenz, M. The Effect of Particle Proximity on the Oxygen
585 Reduction Rate of Size-Selected Platinum Clusters. *Nat. Mater.* **2013**, *12* (10),
586 919–924. https://doi.org/10.1038/nmat3712.
587 (15) Nesselberger, M.; Ashton, S.; Meier, J. C.; Katsounaros, I.; Mayrhofer, K. J. J.;
588 Arenz, M. The Particle Size Effect on the Oxygen Reduction Reaction Activity of
589 Pt Catalysts: Influence of Electrolyte and Relation to Single Crystal Models. *J. Am.*
590 *Chem. Soc.* **2011**, *133* (43). https://doi.org/10.1021/ja207016u.
591 (16) Tritsaris, G. A.; Greeley, J.; Rossmeisl, J.; Nørskov, J. K. Atomic-Scale Modeling
592 of Particle Size Effects for the Oxygen Reduction Reaction on Pt. *Catal. Letters*
593 **2011**, *141* (7), 909–913. https://doi.org/10.1007/s10562-011-0637-8.
594 (17) Holby, E. F.; Sheng, W.; Shao-Horn, Y.; Morgan, D. Pt Nanoparticle Stability in
595 PEM Fuel Cells: Influence of Particle Size Distribution and Crossover Hydrogen.
596 *Energy Environ. Sci.* **2009**, *2* (8), 865. https://doi.org/10.1039/b821622n.
597 (18) Quinson, J.; Inaba, M.; Neumann, S.; Swane, A. A.; Bucher, J.; Simonsen, S. B.;
598 Theil Kuhn, L.; Kirkensgaard, J. J. K.; Jensen, K. M.; Oezaslan, M.; Kunz, S.;
599 Arenz, M. Investigating Particle Size Effects in Catalysis by Applying a Size-
600 Controlled and Surfactant-Free Synthesis of Colloidal Nanoparticles in Alkaline
601 Ethylene Glycol: Case Study of the Oxygen Reduction Reaction on Pt. *ACS Catal.*

602 **2018**, *8* (7), 6627–6635. https://doi.org/10.1021/acscatal.8b00694.

603 (19) Gasteiger, H. A.; Kocha, S. S.; Sompalli, B.; Wagner, F. T. Activity Benchmarks
604 and Requirements for Pt, Pt-Alloy, and Non-Pt Oxygen Reduction Catalysts for
605 PEMFCs. *Applied Catalysis B: Environmental*. 2005, pp 9–35.
606 https://doi.org/10.1016/j.apcatb.2004.06.021.

607 (20) Mayrhofer, K. J. J.; Blizanac, B. B.; Arenz, M.; Stamenkovic, V. R.; Ross, P. N.;
608 Markovic, N. M. The Impact of Geometric and Surface Electronic Properties of
609 Pt-Catalysts on the Particle Size Effect in Electrocatalysis. *J. Phys. Chem. B* **2005**,
610 *109* (30). https://doi.org/10.1021/jp051735z.

611 (21) Mayrhofer, K. J. J.; Strmcnik, D.; Blizanac, B. B.; Stamenkovic, V.; Arenz, M.;
612 Markovic, N. M. Measurement of Oxygen Reduction Activities via the Rotating
613 Disc Electrode Method: From Pt Model Surfaces to Carbon-Supported High
614 Surface Area Catalysts. *Electrochim. Acta* **2008**, *53* (7), 3181–3188.
615 https://doi.org/10.1016/j.electacta.2007.11.057.

616 (22) Shao, M.; Peles, A.; Shoemaker, K. Electrocatalysis on Platinum Nanoparticles:
617 Particle Size Effect on Oxygen Reduction Reaction Activity. *Nano Lett.* **2011**, *11*
618 (9), 3714–3719. https://doi.org/10.1021/nl2017459.

619 (23) Perez-Alonso, F. J.; McCarthy, D. N.; Nierhoff, A.; Hernandez-Fernandez, P.;

Strebel, C.; Stephens, I. E. L.; Nielsen, J. H.; Chorkendorff, I. The Effect of Size on the Oxygen Electroreduction Activity of Mass-Selected Platinum Nanoparticles. *Angew. Chemie - Int. Ed.* **2012**, *51* (19), 4641–4643. https://doi.org/10.1002/anie.201200586.

(24) Bett, J.; Lundquist, J.; Washington, E.; Stonehart, P. Platinum Crystallite Size Considerations for Electrocatalytic Oxygen Reduction-I. *Electrochim. Acta* **1973**, *18* (5), 343–348. https://doi.org/10.1016/0013-4686(73)85002-9.

(25) Sattler, M. L.; Ross, P. N. The Surface Structure of Pt Crystallites Supported on Carbon Black. *Ultramicroscopy* **1986**, *20* (1–2), 21–28. https://doi.org/10.1016/0304-3991(86)90163-4.

(26) Peuckert, M.; Yoneda, T.; Betta, R. A. D.; Boudart, M. Oxygen Reduction on Small Supported Platinum Particles. *J. Electrochem. Soc.* **1986**, *133* (5), 944–947. https://doi.org/10.1149/1.2108769.

(27) Kinoshita, K. Particle Size Effects for Oxygen Reduction on Highly Dispersed Platinum in Acid Electrolytes. *J. Electrochem. Soc.* **1990**, *137* (3), 845–848. https://doi.org/10.1149/1.2086566.

(28) Watanabe, M.; Sei, H.; Stonehart, P. The Influence of Platinum Crystallite Size on the Electroreduction of Oxygen. *J. Electroanal. Chem.* **1989**, *261* (2 PART 2), 375–

638 387. https://doi.org/10.1016/0022-0728(89)85006-5.

639 (29) Bregoli, L. J. The Influence of Platinum Crystallite Size on the Electrochemical

640 Reduction of Oxygen in Phosphoric Acid. *Electrochim. Acta* **1978**, *23* (6), 489–

641 492. https://doi.org/10.1016/0013-4686(78)85025-7.

642 (30) Henry, C. R. Surface Studies of Supported Model Catalysts. *Surf. Sci. Rep.* **1998**,

643 *31* (7–8), 231–233. https://doi.org/10.1016/S0167-5729(98)00002-8.

644 (31) Röttgen, M. A.; Abbet, S.; Judai, K.; Antonietti, J.-M.; Wörz, A. S.; Arenz, M.;

645 Henry, C. R.; Heiz, U. Cluster Chemistry: Size-Dependent Reactivity Induced by

646 Reverse Spill-Over. *J. Am. Chem. Soc.* **2007**, *129* (31), 9635–9639.

647 https://doi.org/10.1021/ja068437f.

648 (32) Cargnello, M. Colloidal Nanocrystals as Building Blocks for Well-Defined

649 Heterogeneous Catalysts. *Chem. Mater.* **2019**, *31* (3), 576–596.

650 https://doi.org/10.1021/acs.chemmater.8b04533.

651 (33) Quinson, J.; Kunz, S.; Arenz, M. Beyond Active Site Design: A Surfactant-Free

652 Toolbox Approach for Optimised Supported Nanoparticle Catalysts.

653 *ChemCatChem* **2021**, *13*, 1692 – 1705.

654 https://doi.org/https://doi.org/10.1002/cctc.202001858.

655 (34) Heiz, U.; Vanolli, F.; Trento, L.; Schneider, W. D. Chemical Reactivity of Size-

656 Selected Supported Clusters: An Experimental Setup. *Rev. Sci. Instrum.* **1997**, *68*
657 (5), 1986–1994. https://doi.org/10.1063/1.1148113.
658 (35) Halder, A.; Curtiss, L. A.; Fortunelli, A.; Vajda, S. Perspective: Size Selected
659 Clusters for Catalysis and Electrochemistry. *J. Chem. Phys.* **2018**, *148* (11).
660 https://doi.org/10.1063/1.5020301.
661 (36) Speder, J.; Altmann, L.; Bäumer, M.; Kirkensgaard, J. J. K.; Mortensen, K.; Arenz,
662 M. The Particle Proximity Effect: From Model to High Surface Area Fuel Cell
663 Catalysts. *RSC Adv.* **2014**, *4* (29), 14971–14978.
664 https://doi.org/10.1039/c4ra00261j.
665 (37) Huang, J.; Zhang, J.; Eikerling, M. H. Particle Proximity Effect in Nanoparticle
666 Electrocatalysis: Surface Charging and Electrostatic Interactions. *J. Phys. Chem.*
667 *C* **2017**, *121* (9), 4806–4815. https://doi.org/10.1021/acs.jpcc.6b10842.
668 (38) Liu, H.; Mun, B. S.; Thornton, G.; Isaacs, S. R.; Shon, Y. S.; Ogletree, D. F.;
669 Salmeron, M. Electronic Structure of Ensembles of Gold Nanoparticles: Size and
670 Proximity Effects. *Phys. Rev. B - Condens. Matter Mater. Phys.* **2005**, *72* (15), 1–
671 5. https://doi.org/10.1103/PhysRevB.72.155430.
672 (39) Murray, C. B.; Kagan, C. R.; Bawendi, M. G. Synthesis and Characterization of
673 Monodisperse Nanocrystals and Close-Packed Nanocrystal Assemblies. *Annu. Rev.*

674 *Mater. Sci.* **2000**, *30*, 545–610. https://doi.org/10.1146/annurev.matsci.30.1.545.
675 (40) Nielsen, R. M.; Murphy, S.; Strebel, C.; Johansson, M.; Chorkendorff, I.; Nielsen,
676 J. H. The Morphology of Mass Selected Ruthenium Nanoparticles from a
677 Magnetron-Sputter Gas-Aggregation Source. *J. Nanoparticle Res.* **2010**, *12* (4),
678 1249–1262. https://doi.org/10.1007/s11051-009-9830-8.
679 (41) Reichenberger, S.; Marzun, G.; Muhler, M.; Barcikowski, S. Perspective of
680 Surfactant-Free Colloidal Nanoparticles in Heterogeneous Catalysis.
681 *ChemCatChem* **2019**, *11* (18), 4489–4518. https://doi.org/10.1002/cctc.201900666.
682 (42) Speder, J.; Zana, A.; Arenz, M. The Colloidal Tool-Box Approach for Fuel Cell
683 Catalysts: Systematic Study of Perfluorosulfonate-Ionomer Impregnation and Pt
684 Loading. *Catal. Today* **2016**, *262*, 82–89.
685 https://doi.org/10.1016/j.cattod.2015.09.021.
686 (43) Wang, Y.; Ren, J.; Deng, K.; Gui, L.; Tang, Y. Preparation of Tractable Platinum,
687 Rhodium, and Ruthenium Nanoclusters with Small Particle Size in Organic Media.
688 *Chem. Mater.* **2000**, *12* (6), 1622–1627. https://doi.org/10.1021/cm0000853.
689 (44) Quinson, J.; Inaba, M.; Neumann, S.; Swane, A. A. A.; Bucher, J.; Simonsen, S.
690 B.; Theil Kuhn, L.; Kirkensgaard, J. J. K.; Jensen, K. M. Ø.; Oezaslan, M.; Kunz,
691 S.; Arenz, M. Investigating Particle Size Effects in Catalysis by Applying a Size-

692 Controlled and Surfactant-Free Synthesis of Colloidal Nanoparticles in Alkaline
693 Ethylene Glycol: Case Study of the Oxygen Reduction Reaction on Pt. *ACS Catal.*
694 **2018**, *8* (7), 6627–6635. https://doi.org/10.1021/acscatal.8b00694.
695 (45) Speder, J.; Altmann, L.; Roefzaad, M.; Bäumer, M.; Kirkensgaard, J. J. K.;
696 Mortensen, K.; Arenz, M. Pt Based PEMFC Catalysts Prepared from Colloidal
697 Particle Suspensions-a Toolbox for Model Studies. *Phys. Chem. Chem. Phys.* **2013**,
698 *15* (10), 3602–3608. https://doi.org/10.1039/c3cp50195g.
699 (46) Inaba, M.; Quinson, J.; Bucher, J. R.; Arenz, M. On the Preparation and Testing of
700 Fuel Cell Catalysts Using the Thin Film Rotating Disk Electrode Method. *J. Vis.*
701 *Exp.* **2018**, *133* (133), e57105. https://doi.org/10.3791/57105.
702 (47) Inaba, M.; Quinson, J.; Arenz, M. PH Matters: The Influence of the Catalyst Ink
703 on the Oxygen Reduction Activity Determined in Thin Film Rotating Disk
704 Electrode Measurements. *J. Power Sources* **2017**, *353*, 19–27.
705 https://doi.org/10.1016/j.jpowsour.2017.03.140.
706 (48) Mayrhofer, K. J. J.; Wiberg, G. K. H.; Arenz, M. Impact of Glass Corrosion on the
707 Electrocatalysis on Pt Electrodes in Alkaline Electrolyte. *J. Electrochem. Soc.* **2008**,
708 *155* (1). https://doi.org/10.1149/1.2800752.
709 (49) Binninger, T.; Fabbri, E.; Patru, A.; Garganourakis, M.; Han, J.; Abbott, D. F.;

Sereda, O.; Kötz, R.; Menzel, A.; Nachtegaal, M.; Schmidt, T. J. Electrochemical Flow-Cell Setup for In Situ X-Ray Investigations. *J. Electrochem. Soc.* **2016**, *163* (10), H906–H912. https://doi.org/10.1149/2.0201610jes.

(50) Newville, M. IFEFFIT: Interactive XAFS Analysis and FEFF Fitting. *J. Synchrotron Radiat.* **2001**, *8* (2), 322–324. https://doi.org/10.1107/S0909049500016964.

(51) Shinozaki, K.; Morimoto, Y.; Pivovar, B. S.; Kocha, S. S. Re-Examination of the Pt Particle Size Effect on the Oxygen Reduction Reaction for Ultrathin Uniform Pt/C Catalyst Layers without Influence from Nafion. *Electrochim. Acta* **2016**, *213*, 783–790. https://doi.org/10.1016/j.electacta.2016.08.001.

(52) Friebel, D.; Miller, D. J.; O'Grady, C. P.; Anniyev, T.; Bargar, J.; Bergmann, U.; Ogasawara, H.; Wikfeldt, K. T.; Pettersson, L. G. M.; Nilsson, A. In Situ X-Ray Probing Reveals Fingerprints of Surface Platinum Oxide. *Phys. Chem. Chem. Phys.* **2011**, *13* (1), 262–266. https://doi.org/10.1039/c0cp01434f.

(53) Nagamatsu, S. I.; Arai, T.; Yamamoto, M.; Ohkura, T.; Oyanagi, H.; Ishizaka, T.; Kawanami, H.; Uruga, T.; Tada, M.; Iwasawa, Y. Potential-Dependent Restructuring and Hysteresis in the Structural and Electronic Transformations of Pt/C, Au(Core)-Pt(Shell)/C, and Pd(Core)-Pt(Shell)/C Cathode Catalysts in

728 Polymer Electrolyte Fuel Cells Characterized by in Situ X-Ray Absorption Fine St.

729 *J. Phys. Chem. C* **2013**, *117* (25), 13094–13107. https://doi.org/10.1021/jp402438e.

730